Journal of Nuclear Materials 480 (2016) 182–188

Contents lists available at ScienceDirect

Journal of Nuclear Materials

journal homepage: www.elsevier.com/locate/jnucmat

Synthesis and radiation tolerance of $Lu_{2-x}Ce_xTi_2O_7$ pyrochlores

Y. Xia, C.G. Liu, D.Y. Yang, J. Wen, H. Liu, P.C. Mu, Y.H. Li*

School of Nuclear Science and Technology, Lanzhou University, Lanzhou, Gansu 730000, China

HIGHLIGHTS

- The maximum solubility of $Ce_2Ti_2O_7$ in $Lu_2Ti_2O_7$ is identified to be 32 mol %.
- The radiation tolerance of $Lu_{2-x}Ce_x$-Ti_2O_7 decreases with increasing cerium content.
- The cation antisite defect formation energy decreases with increasing Ce^{3+} content based on DFT calculations.

GRAPHICAL ABSTRACT

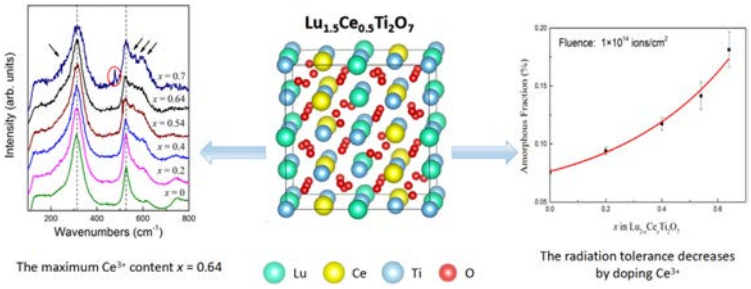

ARTICLE INFO

Article history:
Received 6 April 2016
Received in revised form
17 August 2016
Accepted 22 August 2016
Available online 23 August 2016

Keywords:
Ce doped pyrochlores
Synthesis
Solubility
Ion irradiation
Radiation tolerance

ABSTRACT

As a nonradioactive surrogate for Pu, Ce is selected to study the solubility and radiation tolerance in pyrochlore matrixes. In this paper, we synthesized a series of $Lu_{2-x}Ce_xTi_2O_7$ ($x = 0$–0.7) samples. X-ray diffraction, X-ray photoelectron spectroscopy and Raman spectroscopy were used to study the structure of $Lu_{2-x}Ce_xTi_2O_7$ ($x = 0$–0.7) with different Ce^{3+} content x. The results show that the maximum solubility of Ce^{3+} in $Lu_2Ti_2O_7$ is 32 mol%. In order to study the radiation tolerance of these compounds, 400 keV Ne^{2+} was used to perform the irradiation experiments. The grazing incident X-ray diffraction patterns revealed that the radiation tolerance of the $Lu_{2-x}Ce_xTi_2O_7$ decreases with increasing Ce-content. This correlation between radiation tolerance and Ce-content was interpreted in terms of the antisite defect formation energies of $Lu_{2-x}Ce_xTi_2O_7$ ($x = 0$, 0.5, 1) based on the density functional theory.

1. Introduction

$A_2B_2O_7$ pyrochlore oxides with diverse compositions have been investigated for various technological applications during the last decades [1–7]. Pyrochlores are ordered superstructures of the fluorite (CaF_2) with two cation sites and one-eighth fewer anions, belonging to $Fd\bar{3}m$ space group. The larger A^{3+} cations are eight-coordinated and lie on 16*d* sites. The smaller B^{3+} cations are six-coordinated and occupy 16*c* positions. The anions occupy two sites: the 48*f* oxygen is coordinated to two B^{4+} and two A^{3+} cations, while the 8*b* oxygen is in coordination with four A^{3+} cations. An unoccupied site, 8*a*, is surrounded by four B^{4+} ions, and the "vacancies" are ordered on the anion sublattice [1,2].

Due to the remarkable structural flexibility, compositional diversity and chemical durability, numerous works have been concentrated on pyrochlores as potential matrixes for the immobilization of actinides, particularly Pu, which is created in nuclear reactors around the world [3–7]. The radiation from these highly radioactive actinides can induce diverse microstructural changes, such as amorphization, volume expansion, cracking, and reduced chemical durability. These changes severely affect the long-term performance of the matrixes. Naturally, it is of significant

* Corresponding author.
E-mail address: liyuhong@lzu.edu.cn (Y.H. Li).

http://dx.doi.org/10.1016/j.jnucmat.2016.08.027
0022-3115/

importance to investigate the irradiation effects of the actinide-doped $A_2B_2O_7$ pyrochlore oxides.

A large number of experimental as well as computational studies on the incorporation behavior of actinides in pyrochlores have been reported [4,8–13]. Shoup et al. [4] identified the solubility limits of $Pu_2Ti_2O_7$ in $Gd_2Ti_2O_7$, $Er_2Ti_2O_7$ and $Lu_2Ti_2O_7$ were 16 ± 4, 22 ± 3 and 33 ± 3 mol%, respectively. Since the ionic radius and the electronic configuration of Ce are similar to those of Pu, Ce has often been used as a nonradioactive surrogate for Pu due to safety and security concerns [14–16]. The solubility limits of $Ce_2Ti_2O_7$ in $A_2Ti_2O_7$ (A = Gd, Er, Lu) hosts, which have been studied experimentally by C.E. Bamberger et al. [17], were estimated to be 19, 22 and 27 mol%, respectively. These values were found to be in agreement with the solubility limits of $Pu_2Ti_2O_7$, except the solubility of $Ce_2Ti_2O_7$ in $Lu_2Ti_2O_7$ was a little lower. An empirical function of solubility vs. δ (the percent difference between ionic radii of solute and solvent cations) [18] was used to calculate the solubility of $Ce_2Ti_2O_7$ in $Lu_2Ti_2O_7$, the value was 32 mol% [17]. The discrepancy between calculated value and experimental value was supposed to be the fact that the solubility vs. δ function was based on several interpolations whereas the experimental value was directly derived from measurements [17]. In addition to solubility, the radiation tolerance of Ce-doped $A_2Ti_2O_7$ is also well worth investigating. However, to our best knowledge, only C.E. Bamberger et al. studied the solubility of Ce^{3+} in $Lu_2Ti_2O_7$, while there is still an absence of studies on the irradiation effects of $A_{2-x}Ce_xTi_2O_7$.

In the present study, we prepared a series of Ce-doped $Lu_{2-x}Ce_xTi_2O_7$ (x = 0–0.7) samples. X-ray diffraction (XRD), X-ray photoelectron spectroscopy (XPS) and Raman spectroscopy were applied to study the structural changes and determine the maximum solubility of $Ce_2Ti_2O_7$ in $Lu_2Ti_2O_7$. Furthermore, we first performed the radiation experiments on $Lu_{2-x}Ce_xTi_2O_7$ using 400 keV Ne^{2+} ions at room temperature. The structural evolutions of the irradiated layers were characterized by grazing incident X-ray diffraction (GIXRD). In order to interpret the experimental results, first principle calculations based on the density functional theory (DFT) were performed in the framework of antisite defect formation energies.

2. Experimental

Polycrystalline $Lu_{2-x}Ce_xTi_2O_7$ (x = 0–0.7) pyrochlores were prepared via a solid-state reaction process. Lu_2O_3 (99.99% purity), CeO_2 (99.99% purity), TiO_2 (99.99% purity) and TiN (99.99% purity) were selected as raw materials. TiN was used as the reductant [10,17]. The sequence of reactions can be written as,

$$8CeO_2 + 2TiN \rightarrow 4Ce_2O_3 + 2TiO_2 + N_2\uparrow$$

and

$$xCe_2O_3 + (2-x)Lu_2O_3 + 4TiO_2 \rightarrow 2Lu_{2-x}Ce_xTi_2O_7$$

The mixed powders were ball-milled and pressed into pellets at a pressure of 450 MPa in a 13 mm diameter stainless steel die. The pellets were then sintered at 1500 °C for 24 h under an argon atmosphere. The sintered pellets were reground into powder and repressed into pellets, and then re-sintered at 1500 °C for 48 h under an argon atmosphere subsequently. Finally, the resulting samples were polished to a mirror finished.

The obtained samples were characterized by X-ray diffraction (XRD), X-ray photoelectron spectroscopy (XPS) and Raman spectroscopy. The XRD analysis of the samples was carried out on a Rigaku D/Max-2400 X-ray Diffractometer with Cu-$K\alpha$ radiation of wavelength λ = 1.5406 Å. The XRD patterns were collected in a θ-2θ range of 10–70° with a step size of 0.02° at room temperature and a dwell time of 2 s per step. X-ray photoelectron spectroscopy (XPS) was recorded by the ESCALAB 250Xi (Thermo Fisher Scientific) equipped with 500 mm Rowland circle monochromator. The XPS data from the region related to the Ce 3d core level was recorded for each sample. The binding energies (BE) were adjusted relative to C 1s at 284.7 eV. Room temperature Raman spectroscopy was performed on a Jobin-Yvon Lab Ram 80 HR, equipped with a confocal microscope. The 532 nm line of He-Ne laser was used as an excitation source.

The ion-irradiation experiments were performed in the College of Energy at Xia'men University, using a 400 kV high current research ion implanter. 400 keV Ne^{2+} ions were implanted under normal incidence at fluencies ranging from 1×10^{14} to 2×10^{15} ions/cm^2 (0.04–0.8 dpa) with an average flux of 1.1×10^{12} ions/cm^2·s at room temperature. Using the SRIM-2000 code [19], the range of 400 keV Ne^{2+} ions was estimated to be about 500 nm. In these calculations, the threshold displacement energies for Lu, Ce, Ti and O were all assumed to be 40 eV (these energies were arbitrary assumptions because we currently have not had experimental or theoretical estimates for these values). The irradiated samples were characterized by a Rigaku Ultima IV Advanced diffractometer with Cu-$K\alpha$ radiation. The θ-2θ scans in the range of 10–70° were performed using a step size of 0.02° and a dwell time of 1s per step. X-ray diffraction patterns were recorded at a glancing incident angle of γ = 0.5°. Under this incident angle, X-ray only scatters from the layer of the sample within a depth of about 150 nm, which is significantly shallower than the range of the 400 keV Ne^{2+} ions in $Lu_{2-x}Ce_xTi_2O_7$ (x = 0–0.64) according to SRIM calculation (500 nm). Therefore, only the irradiated layer of $Lu_{2-x}Ce_xTi_2O_7$ (x = 0–0.64) can be detected.

3. Results and discussion

3.1. The maximum solubility of Ce^{3+} in $Lu_2Ti_2O_7$

3.1.1. X-ray diffraction (XRD)

The crystalline phases of the $Lu_{2-x}Ce_xTi_2O_7$ (x = 0–0.7) powders were determined by XRD as shown in Fig. 1. All the patterns display peaks at 2θ ≈ 15, 29, 39, 47 and 54°, corresponding to the (1 1 1), (3 1 1), (3 3 1), (5 1 1) and (5 3 1) miller indices, respectively. These odd (h k l) miller-indexed peaks represent the "superlattice" reflections of pyrochlore structure. From the inset of Fig. 1, one can discern that

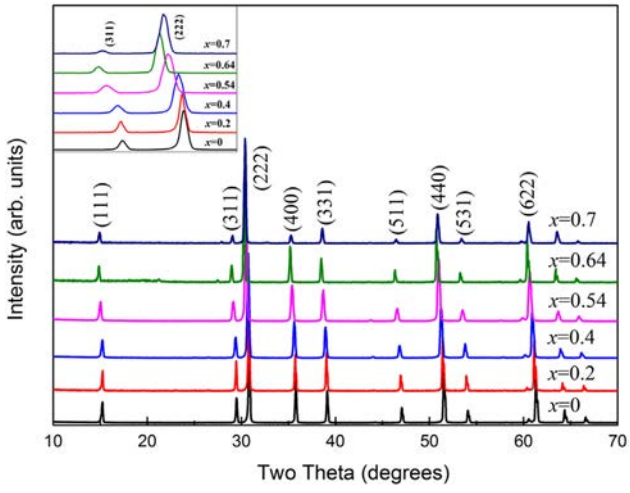

Fig. 1. XRD patterns obtained from pristine $Lu_{2-x}Ce_xTi_2O_7$ (x = 0–0.7) pyrochlores. The inset presents an enlarged view of the 2θ = 28°–32° region.

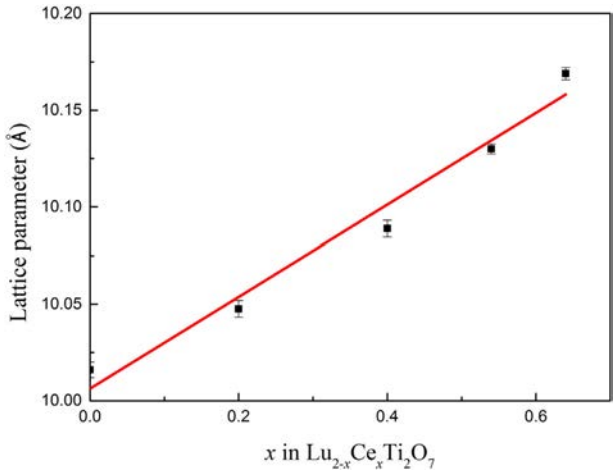

Fig. 2. Lattice parameter of pristine $Lu_{2-x}Ce_xTi_2O_7$ ($x = 0$–0.64) as a function of the cerium doping content x.

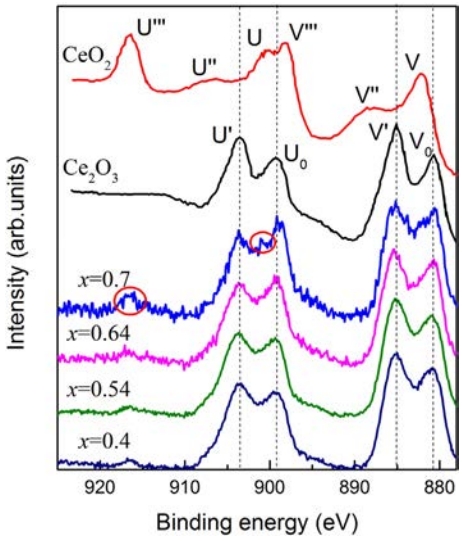

Fig. 3. Ce 3d XPS spectra of $Lu_{2-x}Ce_xTi_2O_7$ ($x = 0.4$–0.7), the data were normalized. The spectra of CeO_2 and Ce_2O_3 are also presented as a contrast.

all the diffraction peaks shift towards smaller 2θ with increasing x from 0 to 0.64, while for the composition of $x = 0.7$, all the peaks shift to larger 2θ. According to the previous studies [20–23], the shift of the peaks towards smaller 2θ indicates the lattice parameter of the $Lu_{2-x}Ce_xTi_2O_7$ ($x = 0$–0.64) increases with increasing x. In contrast, the lattice parameter of $Lu_{1.3}Ce_{0.7}Ti_2O_7$ decreases, which implies that the Ce was not completely incorporated into the $Lu_2Ti_2O_7$ pyrochlore in trivalence. To investigate the variation quantitatively, the lattice parameters of $Lu_{2-x}Ce_xTi_2O_7$ ($x = 0$–0.64) were calculated by Bragg's law based on four primary peaks with even indices in XRD patterns: (2 2 2), (4 0 0), (4 4 0) and (6 2 2). The relationship between lattice parameter and the Ce content x in $Lu_{2-x}Ce_xTi_2O_7$ is depicted in Fig. 2. It is worth noting that the lattice parameter increases almost linearly with increasing doped-Ce content. In previous study, the lattice parameter generally exhibits an approximately linear increase when the smaller cation is replaced by a larger one [24], which means the increased lattice parameter of samples with higher x values can be attributed to the incorporation of atoms with larger ionic radius. Since the ionic radius of Lu^{3+} and Ce^{3+} with eight-coordination is 0.997 and 1.143 nm, respectively, whereas the radius of Ce^{4+} with six-coordination is 0.87 nm, the lattice parameter would increase if Ce^{3+} was doped into A-site. In contrast, the lattice parameter would decrease if Ce^{4+} was doped into B-site. Combining with Fig. 1, it can be concluded that the incorporated Ce ions present trivalence predominantly. The approximately linear increase of the lattice parameter with increasing Ce incorporation content x indicates that Ce^{3+} ions have been doped into A-site of compounds.

3.1.2. X-ray photoelectron spectroscopy (XPS)

For the purpose of obtaining further valence information of Ce, XPS was applied to characterize these samples. As a transition-metal, Ce 3d XPS spectrum is highly sensitive to the coordination numbers of Ce. Therefore, the XPS spectrum of Ce 3d can reflect the coordination numbers of Ce, which changes with the interaction between supporter and Ce [25,26]. According to the literature by X. Wang et al. [22], the Ce_2O_3 spectrum (representing Ce^{3+}) is labeled with V_0, V′ and U_0, U′, V′ and U′, representing the binding energy intensities of the $3d_{5/2}$ and $3d_{3/2}$ for $4f^1$, $4f^2$ configuration. Correspondingly, V, V″, V‴ and U, U″, U‴ describe the $3d_{5/2}$ and $3d_{3/2}$ photoelectron intensities for $4f^2$, $4f^1$ and $4f^0$ occupation in CeO_2 (representing Ce^{4+}) [27]. In this work, the Ce is expected to be doped into A-site, namely, Ce should be in trivalence in the compounds. The XPS spectra of Ce in $Lu_{2-x}Ce_xTi_2O_7$ ($x = 0.4$–0.7) are illustrated in Fig. 3. Comparing the observed 3d envelop with those previously reported for Ce^{3+} and Ce^{4+} [22,25–27], it is found that all the spectra of $Lu_{2-x}Ce_xTi_2O_7$ ($x = 0.4$–0.64) samples are closely consistent with the Ce 3d spectrum of Ce_2O_3. On the other hand, as the red circles marked, peaks belonging to Ce^{4+} oxidation states occur in $Lu_{1.3}Ce_{0.7}Ti_2O_7$. Additionally, no obvious change was observed in Ce 3d spectrum for $Lu_{2-x}Ce_xTi_2O_7$ ($x = 0.4$–0.64), which implies that the coordination numbers of Ce did not change when $x \leq 0.64$. Hence, Ce in $Lu_{2-x}Ce_xTi_2O_7$ ($x = 0.4$–0.64) compounds that we have synthesized is in trivalence predominantly, in line with the XRD results above.

3.1.3. Raman spectroscopy

The Raman spectrum of $A_2B_2O_7$ pyrochlores consists of six active Raman modes: A_{1g}, E_{1g}, and four F_{2g} [28,29]. Fig. 4 presents Raman spectra of $Lu_{2-x}Ce_xTi_2O_7$ ($x = 0$–0.7) pristine samples. For $Lu_2Ti_2O_7$, the most prominent band, observed at 312 cm^{-1}, is attributed to the O-Lu-O bending mode, and the band centered at 526 cm^{-1}, is assigned to the Lu-O stretching mode. These wave numbers of the vibrational modes are in accordance with previous studies [30–32]. Four new bands at about 258, 555, 575 and 600 cm^{-1} gradually arise with increasing Ce content x (indicated by the black arrows), which implies that these peaks are correlated with Ce doping. The specific meaning of these peaks is still under DFT calculations and will not be discussed here. Xiaoyan Shu et al. [33] found an additional band at about 480 cm^{-1} as Ce was introduced into the B site of $(Gd_{1-x}Nd_x)_2Zr_2O_7$ pyrochlores. It is worth noting that this band is also observed in the Raman scattering spectrum of $Lu_{1.3}Ce_{0.7}Ti_2O_7$ composition (marked with the red circle). The band is assigned to the vibration of Ce-O, which roots in the substitution in B position [34]. In conclusion, combined with XRD and XPS results, the maximum doping content of Ce^{3+} in $Lu_{2-x}Ce_xTi_2O_7$ is identified to be $x = 0.64$. The result is conformed with the solubility obtained from the empirical function by C.E. Bamberger et al. [18], and close to the solubility of $Pu_2Ti_2O_7$ in $Lu_2Ti_2O_7$ [4].

3.2. Radiation effects of $Lu_{2-x}Ce_xTi_2O_7$

3.2.1. Grazing incident X-ray diffraction pattern

Fig. 5 displays the GIXRD patterns obtained from $Lu_{2-x}Ce_xTi_2O_7$

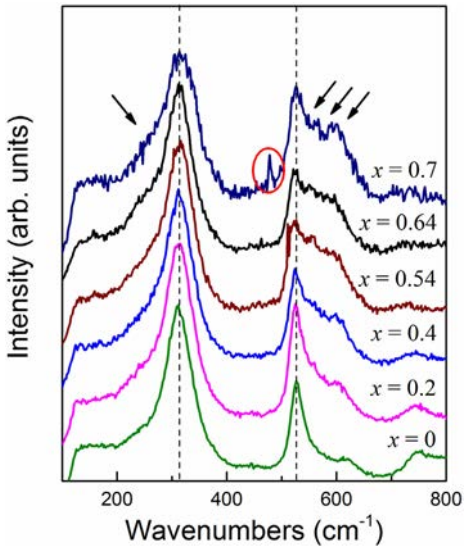

Fig. 4. Raman spectra of pristine $Lu_{2-x}Ce_xTi_2O_7$ ($x = 0$–0.7). The bands rise with increasing Ce content x (as the arrows show), indicating a correlation with the variation mode of Ce in the compounds. The band in the red circle of $Lu_{1.3}Ce_{0.7}Ti_2O_7$ is the vibration of Ce-O, which roots in the substitution in B position. (For interpretation of the references to colour in this figure legend, the reader is referred to the web version of this article.)

($x = 0$–0.64) samples irradiated with 400 keV Ne^{2+} at fluences of 1×10^{14}, 5×10^{14}, 1×10^{15} and 2×10^{15} ions/cm^2, with the X-ray incidence angle of $\gamma = 0.5°$. The diffraction patterns were normalized for clarity.

As shown in Fig. 5(a), the peaks shift towards smaller 2θ with increasing x at fluence of 1×10^{14} ions/cm^2 (~0.04 dpa), indicating that the lattice parameter of $Lu_{2-x}Ce_xTi_2O_7$ ($x = 0$–0.64) increases, which is in accordance with that of the unirradiated samples. No phase transformation (pyrochlore to fluorite transition or amorphization) is observed at this fluence in any of the compounds. At the fluence of 5×10^{14} ions/cm^2 (~0.2 dpa) in Fig. 5(b), the GIXRD patterns show the amorphous fraction significantly increases when Ce content $x \geq 0.4$. Fig. 5(c) illustrates the patterns at the fluence of 1×10^{15} ions/cm^2 (~0.4 dpa). For $Lu_2Ti_2O_7$ ($x = 0$), most superlattice peaks diminished while the fluorite peaks still remained. Simultaneously, the diffuse scattering of the amorphous phase is apparent for other samples. When the fluence reaches 2×10^{15} ions/cm^2 (~0.8 dpa), as depicted in Fig. 5(d), the XRD patterns of all the compounds are predominately contributed by amorphous diffuse scatterings. Moreover, the fraction of the amorphous phase becomes higher with increasing Ce content x, which means that the radiation tolerance decreases with increasing x for $Lu_{2-x}Ce_xTi_2O_7$ ($x = 0$–0.64).

A quantitative analysis of the amorphous fraction as a function of Ce content x was performed. From Fig. 5, we found that the amorphization degree rises with increasing Ce doping content at the same fluence. As an example, here we present the amorphous fraction derived from Fig. 5(a), which shows a more obvious tendency. The fraction of the amorphous phase was extracted using a peak-fitting procedure [35] from the XRD patterns, as displayed in Fig. 6(a). The XRD pattern was deconvoluted into four contributions, consisting of three sharp peaks, corresponding to the (3 1 1), (2 2 2) and (4 0 0) diffracting planes, and a diffuse broad peak arising from the amorphous regions. The amorphous fraction of $Lu_{2-x}Ce_xTi_2O_7$ ($x = 0$–0.64) at the fluence 1×10^{14} ions/cm^2 is shown in Fig. 6(b), which increases with increasing Ce content. Associated with Fig. 5, it demonstrates that the amorphization

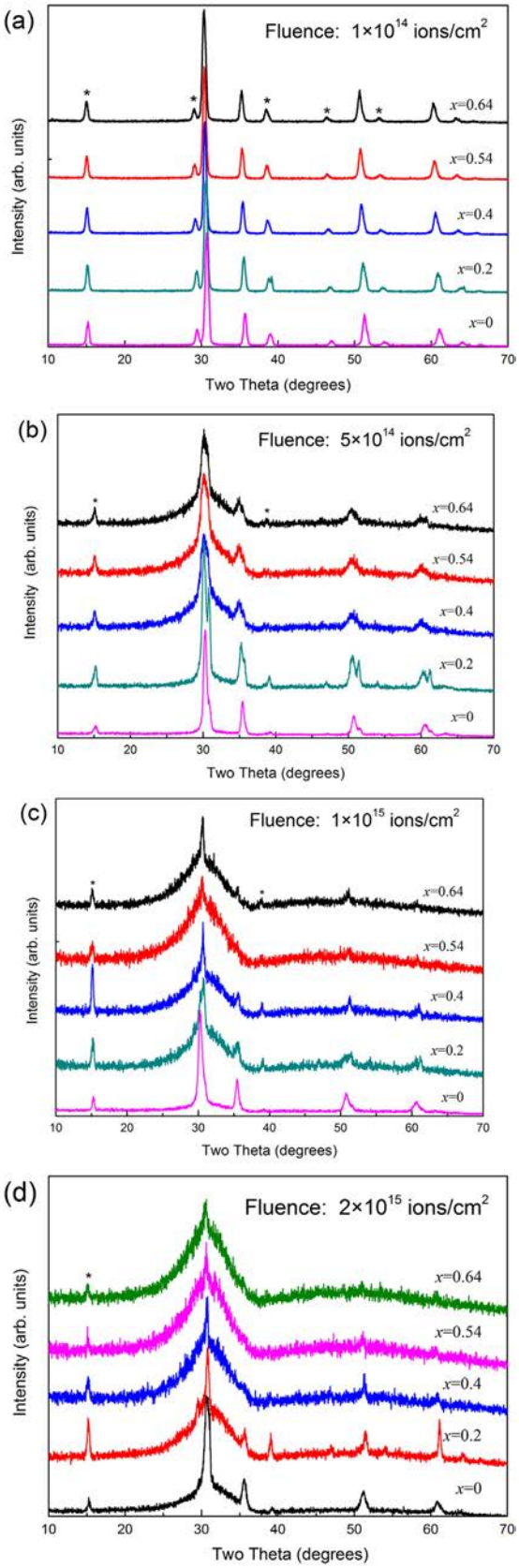

Fig. 5. Normalized GIXRD patterns of $Lu_{2-x}Ce_xTi_2O_7$ ($x = 0$–0.64) irradiated with 400 keV Ne^{2+} ions at the fluence of (a) 1×10^{14} ions/cm^2 (~0.04 dpa), (b) 5×10^{14} ions/cm^2 (~0.2 dpa), (c) 1×10^{15} ions/cm^2 (~0.4 dpa), (d) 2×10^{15} ions/cm^2 (~0.8 dpa).

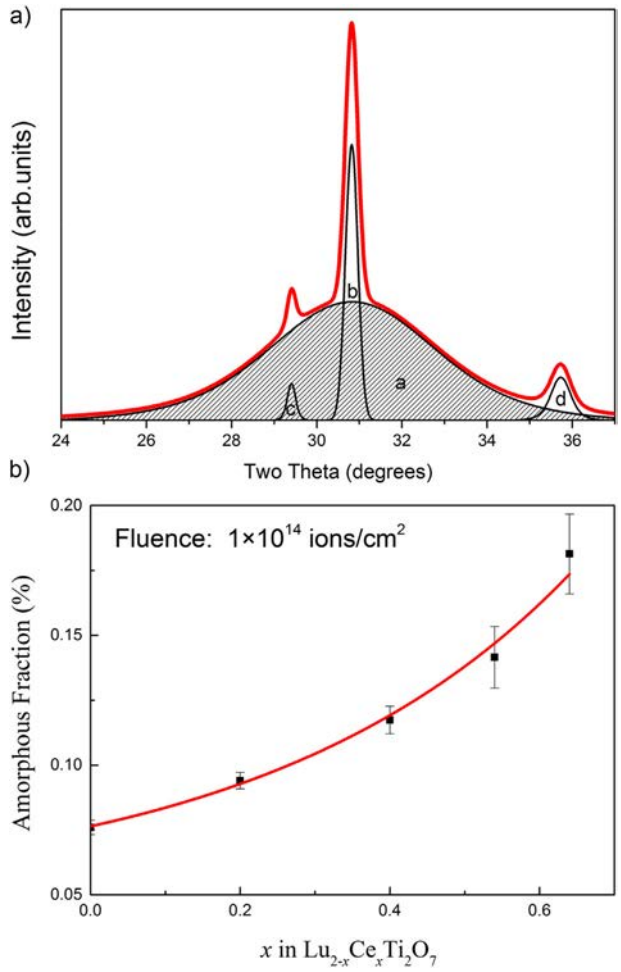

Fig. 6. (a) XRD pattern of $Lu_{1.8}Ce_{0.2}Ti_2O_7$ after irradiating with 2×10^{15} ions/cm^2 (red, solid curve) in the 2θ region of the strongest diffraction peak. The pattern can be deconvoluted into four different contributions of three crystalline maxima (solid curves) and a broad amorphous peak (solid, semi-filled curve). The amorphous sample fraction is determined by the peak-area ratio a/(a + b + c + d). (b) The amorphous fraction as a function of the cerium content x at the fluence of 1×10^{14} ions/cm^2. (For interpretation of the references to colour in this figure legend, the reader is referred to the web version of this article.)

fraction of these samples increase with increasing Ce content at the same fluence. Consequently, we can conclude that the radiation tolerance of the compounds is reduced by doping Ce into the A-site of $Lu_2Ti_2O_7$.

3.2.2. Antisite defect formation energy calculations

To understand the relationship between the radiation tolerance and Ce content x in $Lu_{2-x}Ce_xTi_2O_7$ compounds, the density functional theory (DFT) calculations were performed. From previous literature [23,36–40], the cation antisite is the most stable defect in the pyrochlore structure, and the disordering of cations makes the pyrochlore structure more like a defective fluorite structure. The formation energy of cation antisites in pyrochlores ($A_2B_2O_7$) is one of the important factors that govern the susceptibility to amorphization under irradiations [41]. So that DFT calculations of antisite energies can provide insights into the radiation tolerance of $Lu_{2-x}Ce_xTi_2O_7$ ($x = 0, 0.5, 1.0$) pyrochlores.

The calculations were performed with the Vienna Ab Initio Simulation Package (VASP), applying the projector augmented wave method [41–45]. The generalized gradient approximation (GGA), parametrized by Perdew and Wang, is adopted to treat the exchange-correlation effects [46]. The lattice parameters and internal atomic positions of all structures are fully relaxed using a conjugate gradient scheme. The calculations were based on a unit cell consisting of 88 atoms. The *f*-electrons of lanthanide elements in these compositions are kept frozen in the core [47, 48]. Computations were performed with $2 \times 2 \times 2$ *k*-point sampling in reciprocal space and a cutoff energy of 550 eV for the plane wave basis set, with spin-polarized effects considered. In order to investigate Ce behavior in $Lu_2Ti_2O_7$ pyrochlore, Lu is replaced by Ce at different concentrations, resulting in $Lu_{2-x}Ce_xTi_2O_7$ ($x = 0, 0.5, 1.0$). A full structural relaxation of $Lu_2Ti_2O_7$ with different Ce content was performed. Each composition is found to be energetically stable. $Lu_{1.5}Ce_{0.5}Ti_2O_7$ is taken as an illustration to show the crystal structure and the defect types of the compounds clearly. The configurations of the initial $Lu_{1.5}Ce_{0.5}Ti_2O_7$ pyrochlore structure is displayed in Fig. 7(a), while the Lu-Ti antisite defect and the Ce-Ti antisite defect in $Lu_{1.5}Ce_{0.5}Ti_2O_7$ are illustrated in Fig. 7(b) and(c), respectively.

The formation energy of cation-antisite defects were calculated by:

$$E_F^{AS_{pair}} = E^{AS_{pair}} - E_{tot}$$

Where $E^{AS_{pair}}$ is the total energy of the supercell with AS_{pair}, and E_{tot} is the total energy of the perfect supercell pyrochlore structure [49].

The formation energies of cation antisite defects were calculated and the results are summarized in Table 1. Note that the Lu-Ti cation antisite defect formation energy increases from 1.06 eV to 1.83 eV with increasing Ce content in $Lu_{2-x}Ce_xTi_2O_7$ ($x = 0, 0.5, 1.0$). Meanwhile, all the cation antisite defect formation energies in $Lu_{2-x}Ce_xTi_2O_7$ ($x = 0.5, 1.0$) are apparently higher than that in

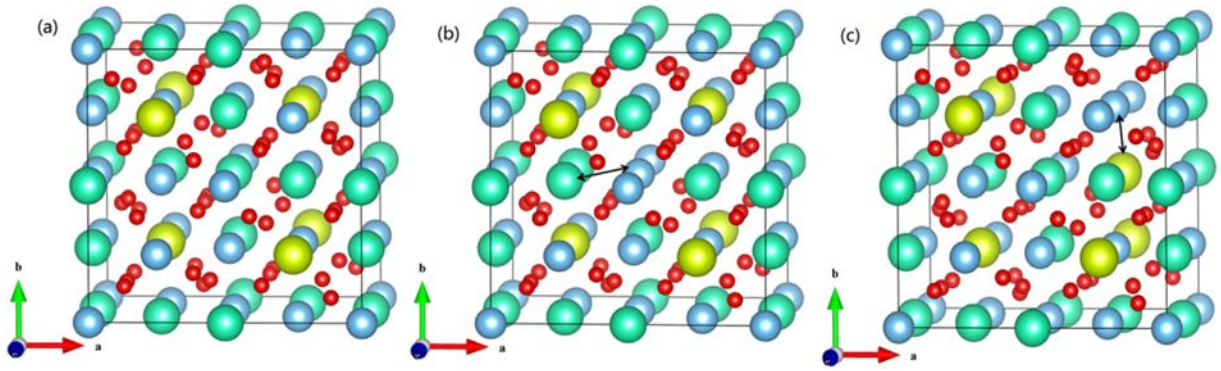

Fig. 7. The unit cell of $Lu_{1.5}Ce_{0.5}Ti_2O_7$, (a) the initial structure, (b) the structure with Lu-Ti antisite defect, (c) the structure with Ce-Ti antisite defect. Green, yellow, blue, and red colors represent lutecium, cerium, titanium, and oxygen atoms, respectively. (For interpretation of the references to colour in this figure legend, the reader is referred to the web version of this article.)

Table 1
Calculated cation antisite defect formation energies (eV) for $Lu_{2-x}Ce_xTi_2O_7$ ($x = 0$, 0.5, 1.0).

Cerium content x	Cation antisite defect formation energy (eV)	
	Ce-Ti antisite defect	Lu-Ti antisite defect
0	–	1.06
0.5	1.71	1.67
1.0	1.48	1.83

$Lu_2Ti_2O_7$. Generally, pyrochlores with lower cation antisite defect formation energies are easier to form a defective fluorite structure and possess a better radiation resistance. According to the calculation results, Ce incorporation in $Lu_2Ti_2O_7$ can increase the cation antisite defect formation energy, and thereby, lead to a decreased radiation resistance, which is consistent with our experimental results.

4. Conclusions

In summary, a series of $Lu_{2-x}Ce_xTi_2O_7$ ($x = 0$–0.7) compounds have been synthesized. The Ce ions were doped into A-site in trivalence successfully, and the maximum doping content of Ce is $x = 0.64$. The GIXRD patterns of the irradiated samples reveal that the radiation tolerance decreases with increasing Ce content x in $Lu_{2-x}Ce_xTi_2O_7$. The DFT calculations give an evident interpretation for the experimental observations. It is demonstrated that doping Ce^{3+} into the A-site of $Lu_2Ti_2O_7$ pyrochlore can increase the formation energies of both Lu-Ti and Ce-Ti antisite defects in $Lu_{2-x}Ce_xTi_2O_7$ pyrochlores, which contributes primarily to the reduction of radiation tolerance of compounds. This work also yields a basis for predicting the radiation response of Pu in $Lu_2Ti_2O_7$ pyrochlore and related materials.

Acknowledgement

This work was supported by the National Natural Science Foundation of China (No. 11475076) and the Fundamental Research Funds for the Central Universities of China (Lanzhou University, lzujbky-2015-bt07). J. Zhang and Q.R. Xie at College of Energy of Xiamen University are gratefully acknowledged for providing the ion irradiation support.

References

[1] M. Subramanian, G. Aravamudan, G.S. Rao, Oxide pyrochlores—a review, Prog. Solid State Chem. 15 (1983) 55–143.
[2] B.C. Chakoumakos, Systematics of the pyrochlore structure type, ideal $A_2B_2X_6Y$, J. Solid State Chem. 53 (1984) 120–129.
[3] W.J. Weber, R.C. Ewing, C. Catlow, T.D. De La Rubia, L. Hobbs, C. Kinoshita, H. Matzke, A. Motta, M. Nastasi, E. Salje, Radiation effects in crystalline ceramics for the immobilization of high-level nuclear waste and plutonium, J. Mater. Res. 13 (1998) 1434–1484.
[4] S.S. Shoup, C.E. Bamberger, R.G. Haire, Novel Plutonium Titanate Compounds, Solid Solutions, $Pu_2Ti_2O_7$-$Ln_2Ti_2O_7$: relevance to nuclear waste disposal, J. Am. Ceram. Soc. 79 (1996) 1489–1493.
[5] S.X. Wang, B. Begg, L.M. Wang, R.C. Ewing, W.J. Weber, K.G. Kutty, Radiation stability of gadolinium zirconate: a waste form for plutonium disposition, J. Mater. Res. 14 (1999) 4470–4473.
[6] W.J. Weber, R.C. Ewing, Plutonium immobilization and radiation effects, Science 289 (2000) 2051–2052.
[7] R.C. Ewing, W.J. Weber, J. Lian, Nuclear waste disposal—Pyrochlore ($A_2B_2O_7$): nuclear waste form for the immobilization of plutonium and "minor" actinides, J. Appl. Phys. 95 (2004) 5949–5971.
[8] K.G. Kutty, R. Asuvathraman, R.R. Madhavan, H. Jena, Actinide immobilization in crystalline matrix: a study of uranium incorporation in gadolinium zirconate, J. Phys. Chem. Solids 66 (2005) 596–601.
[9] A. Cleave, R.W. Grimes, K. Sickafus, Plutonium and uranium accommodation in pyrochlore oxides, Philos. Mag. 85 (2005) 967–980.
[10] N. Kulkarni, S. Sampath, V. Venugopal, Preparation and characterisation of Pu-pyrochlore: (La1−xPux)2Zr2O7 (x= 0–1), J. Nucl. Mater. 281 (2000) 248–250.
[11] J. Lian, F.X. Zhang, M.T. Peters, L.M. Wang, R.C. Ewing, Ion beam irradiation of lanthanum and thorium-doped yttrium titanates, J. Nucl. Mater. 362 (2007) 438–444.
[12] P.E. Raison, R.G. Haire, T. Sato, T. Ogawa, Fundamental and technological aspects of actinide oxide pyrochlores: relevance for immobilization matrices, in: MRS Proceedings, vol. 556, Cambridge Univ Press, 1999, p. 3.
[13] C. Nästren, R. Jardin, J. Somers, M. Walter, B. Brendebach, Actinide incorporation in a zirconia based pyrochlore $(Nd_{1.8}An_{0.2})Zr_2O_{7+x}$ (An = Th, U, Np, Pu, Am), J. Solid State Chem. 182 (2009) 1–7.
[14] S. Patwe, A. Tyagi, Solubility of $Ce^{4+}$and Sr^{2+} in the pyrochlore lattice of $Gd_2Zr_2O_7$ for simulation of Pu and alkaline earth metal, Ceram. Int. 32 (2006) 545–548.
[15] L. Saraf, C.M. Wang, V. Shutthanandan, Y. Zhang, O. Marina, D.R. Baer, S. Thevuthasan, P. Nachimuthu, D.W. Lindle, Oxygen transport studies in nanocrystalline ceria films, J. Mater. Res. 20 (2005) 1295–1299.
[16] X. Wang, H. Xiao, X. Zu, W.J. Weber, Study of cerium solubility in $Gd_2Zr_2O_7$ by DFT+U calculations, J. Nucl. Mater. 419 (2011) 105–111.
[17] C. Bamberger, T. Haverlock, S. Shoup, O. Kopp, N.A. Stump, Compounds of cerium, titanium and oxygen, J. Alloys. Compd. 204 (1994) 101–107.
[18] C. Bamberger, H. Dunn, G. Begun, S. Landry, Substitutional solid solutions from heterotypic lanthanide dititanates $Ln_{2-x}LnxTi_2O_7$, J. Less-Common Met. 109 (1985) 209–217.
[19] J.F. Ziegler, J. Biersack, U. Littmark, The Stopping and Range of Ions in Solids, Vol. 1, Pergamon, New York, 1985.
[20] Y.H. Li, Y.Q. Wang, M. Zhou, C.P. Xu, J. Valdez, K. Sickafus, Light ion irradiation effects on stuffed $Lu_2(Ti_{2-x}Lu_x)O_{7-x/2}$ ($x = 0$, 0.4 and 0.67) structures, Nucl. Instrum. Meth. B 269 (2011) 2001–2005.
[21] D.Y. Yang, C.G. Liu, K.Q. Zhang, Y. Xia, L.J. Chen, H. Liu, Y.H. Li, 2.7 MeV Ar^{11+} ion irradiation induced structural evolution in $Lu_2(Ti_{2-x}Lu_x)O_{7-x/2}$ pyrochlores, J. Nucl. Mater. 466 (2015) 496–501.
[22] X. Wang, K. Jiang, L. Zhou, Characterization and phase stability of pyrochlore $(Nd_{1-x}Ce_x)_2Zr_2O_{7+y}$ (x = 0-1), J. Nucl. Mater. 458 (2015) 156–161.
[23] Y.H. Li, B.P. Uberuaga, C. Jiang, S. Choudhury, J. Valdez, M. Patel, J. Won, Y.-Q. Wang, M. Tang, D. Safarik, Role of antisite disorder on preamorphization swelling in titanate pyrochlores, Phys. Rev. Lett. 108 (2012) 195504.
[24] Z.G. Liu, J.H. Ouyang, Y. Zhou, Heat capacity measurements on $Yb_xGd_{2-x}Zr_2O_7$ ($x = 0$, 1, 2) ceramics by differential scanning calorimetry, B. Mater. Sci. 32 (2009) 603–606.
[25] S. Damyanova, C. Perez, M. Schmal, J. Bueno, Characterization of ceria-coated alumina carrier, Appl. Catal. A-Gen 234 (2002) 271–282.
[26] Y. Zhang, F. Hou, Y. Tan, CeO_2 nanoplates with a hexagonal structure and their catalytic applications in highly selective hydrogenation of substituted nitroaromatics, Chem. Commun. 48 (2012) 2391–2393.
[27] P. Burroughs, A. Hamnett, A.F. Orchard, G. Thornton, Satellite structure in the X-ray photoelectron spectra of some binary and mixed oxides of lanthanum and cerium, J. Chem. Soc. Dalton Trans. (1976) 1686–1698.
[28] G. Sattonnay, C. Legros, S. Moll, L. Thome, C. Decorse, P. Simon, J. Jagielski, I. Jozwik, I. Monnet, Phase transformations induced by high electronic excitation in ion-irradiated $Gd_2(ZrxTi1\text{-}x)_2O_7$ pyrochlores, J. Appl. Phys. 108 (2010).
[29] T. Lummen, I. Handayani, M. Donker, D. Fausti, G. Dhalenne, P. Berthet, A. Revcolevschi, P. van Loosdrecht, Phonon and crystal field excitations in geometrically frustrated rare earth titanates, Phys. Rev. B 77 (2008) 214–310.
[30] B.R. Li, H.B. Chang, H. Gao, S.X. Hou, Synthesis of $Lu_2Ti_2O_7$ nano-rods from molten salt with two-step calcinations, Mater. Lett. 79 (2012) 219–221.
[31] S. Saha, S. Singh, B. Dkhil, S. Dhar, R. Suryanarayanan, G. Dhalenne, A. Revcolevschi, A. Sood, Temperature-dependent Raman and X-ray studies of the spin-ice pyrochlore $Dy_2Ti_2O_7$ and non-magnetic pyrochlore $Lu_2Ti_2O_7$, Phys. Rev. B 78 (2008), 214–102.
[32] S. Kumar, H.C. Gupta, First principles study of zone centre phonons in rare-earth pyrochlore titanates, $RE_2Ti_2O_7$ (RE = Gd, Dy, Ho, Er, Lu; Y), Vib. Spectrosc. 62 (2012) 180–187.
[33] X. Shu, L. Fan, X. Lu, Y. Xie, Y. Ding, Structure and performance evolution of the system $(Gd_{1-x}Nd_x)_2(Zr_{1-y}Ce_y)_2O_7$ ($0 \le x, y \le 1.0$), J. Eur. Ceram. Soc. 35 (2015) 3095–3102.
[34] F. Poulsen, M. Glerup, P. Holtappels, Structure, Raman spectra and defect chemistry modelling of conductive pyrochlore oxides, Solid State Ionics 135 (2000) 595–602.
[35] M. Lang, F.X. Zhang, R.C. Ewing, J. Lian, C. Trautmann, Z. Wang, Structural modifications of $Gd_2Zr_{2-x}Ti_xO_7$ pyrochlore induced by swift heavy ions: disordering and amorphization, J. Mater. Res. 24 (2009) 1322–1334.
[36] J. Lian, W.J. Weber, W. Jiang, L.M. Wang, L.A. Boatner, R.C. Ewing, Radiation-induced effects in pyrochlores and nanoscale materials engineering, Nucl. Instr. Meth. B 250 (2006) 128–136.
[37] J. Lian, L.M. Wang, S.X. Wang, J. Chen, L. Boatner, R. Ewing, Nanoscale manipulation of pyrochlore: new nanocomposite ionic conductors, Phys. Rev. Lett. 87 (2001) 145901.
[38] K.E. Sickafus, R.W. Grimes, J.A. Valdez, A. Cleave, M. Tang, M. Ishimaru, S.M. Corish, C.R. Stanek, B.P. Uberuaga, Radiation-induced amorphization resistance and radiation tolerance in structurally related oxides, Nat. Mater. 6 (2007) 217–223.
[39] J. Lian, J. Chen, L.M. Wang, R.C. Ewing, J.M. Farmer, L.A. Boatner, K. Helean, Structure, structural phase transitions, mechanical properties, defects, etc.-Radiation-induced amorphization of rare-earth titanate pyrochlores, Phys. Rev. B 68 (2003), 134107–134107.

[40] J. Lian, L.M. Wang, J. Chen, K. Sun, R. Ewing, J.M. Farmer, L. Boatner, The order–disorder transition in ion-irradiated pyrochlore, Acta Mater 51 (2003) 1493–1502.
[41] B. Uberuaga, C. Jiang, C. Stanek, K. Sickafus, C. Scott, R. Smith, Prediction of irradiation spectrum effects in pyrochlores, JOM 66 (2014) 2578–2582.
[42] G. Kresse, J. Furthmüller, Efficiency of ab-initio total energy calculations for metals and semiconductors using a plane-wave basis set, Comput. Mater. Sci. 6 (1996) 15–50.
[43] G. Kresse, J. Furthmüller, Efficient iterative schemes for ab initio total-energy calculations using a plane-wave basis set, Phys. Rev. B 54 (1996) 11169.
[44] P.E. Blöchl, Projector augmented-wave method, Phys. Rev. B 50 (1994) 17953.
[45] G. Kresse, D. Joubert, From ultrasoft pseudopotentials to the projector augmented-wave method, Phys. Rev. B 59 (1999) 1758.
[46] J.P. Perdew, J. Chevary, S. Vosko, K.A. Jackson, M.R. Pederson, D. Singh, C. Fiolhais, Atoms, molecules, solids, and surfaces: applications of the generalized gradient approximation for exchange and correlation, Phys. Rev. B 46 (1992) 6671.
[47] H.Y. Xiao, L.M. Wang, X.T. Zu, J. Lian, R.C. Ewing, Theoretical investigation of structural, energetic and electronic properties of titanate pyrochlores, J. Phys. Condens. Matter 19 (2007) 346203.
[48] C.G. Liu, L.J. Chen, D.Y. Yang, J. Wen, L.Y. Dong, Y.H. Li, The “bimodal effect” of the bulk modulus of rare-earth titanate pyrochlore, Comput. Mater. Sci. 114 (2016) 233–235.
[49] H.Y. Xiao, F. Gao, W.J. Weber, Threshold displacement energies and defect formation energies in $Y_2Ti_2O_7$, J. Phys. Condens. Matter. 22 (2010) 415801.